Nanoscale fracture in graphene

Sachin S. Terdalkar [a], Shan Huang [b], Hongyan Yuan [c], Joseph J. Rencis [a], Ting Zhu [b], Sulin Zhang [c,*]

[a] Department of Mechanical Engineering, University of Arkansas, Fayetteville, AR 72701, United States
[b] Woodruff School of Mechanical Engineering, Georgia Institute and Technology, Atlanta, GA 30332, United States
[c] Department of Engineering Science and Mechanics, The Pennsylvania State University, University Park, PA 16802, United States

ARTICLE INFO

ABSTRACT

Fracture of a monolayer graphene is governed by the competition between bond breaking and bond rotation at a crack tip. Using atomistic reaction pathway calculations, we identify a kinetically favorable fracture path that features an alternating sequence of bond rotation and bond breaking. Our results suggest that the mechanical cracking can create fracture edges with nanoscale morphologies due to the non-uniform bond deformation and rupture induced by the localized high stresses near the crack tip. Such fractured edges may provide a structural basis of tailoring the electronic properties of graphene either intrinsically or by further edge functionalization.

© 2010 Published by Elsevier B.V.

Graphene, a monolayer of carbon atoms, is a material with unique low-dimensional physics and potential applications in nano-electronics [1]. It is intrinsically brittle at room temperature, manifested by, for example, catastrophic fracture during the indentation of a freestanding graphene membrane [2]. This brittleness presents a limiting factor for the nano-electro-mechanical applications of graphene [3]. On the positive side, fracture of graphene may be exploited to produce nano-ribbons from a large sample in order that graphene exhibits a sizable energy band gap [4]. A fundamental understanding of the fracture mechanisms in graphene is not only scientifically interesting, but also practically important for preventing or controlling fracture in graphene [5].

Studies on carbon nanotube (CNT), the rolled counterpart of graphene, suggest that the fracture in a honeycomb lattice of graphene may take two distinct routes [6–16]: brittle cleavage rupture or ductile failure by plastic flow instability. The activation of these two fracture mechanisms is mediated by temperature and loading rate. Because of the short-ranged covalent bonding between the sp² hybridized carbon atoms, the deformation of graphene generally involves the localized processes of bond breaking or bond rotation, whereas the sublimation by evaporation of carbon atoms can occur at high temperatures. Here we consider the brittle versus ductile responses of graphene by focusing on the competition between the bond breaking and rotation at a crack tip. In general, at low temperatures, brittle fracture *via* bond breaking prevails, leading to the formation of large open-ring structures [16], whereas at elevated temperatures, plastic deformation dominates, proceeding by nucleation and motion of the Stone–Wales (SW) defect [17], a 5/7–7/5 dislocation dipole formed via rotation of a C–C bond by 90°. Despite of the central importance of the

above two bond transformation modes in fracture, they have not been studied for a crack in graphene.

In this Letter, we aim to elucidate the atomic-scale mechanisms of fracture in graphene. We were able to precisely control the competing fracture pathways in atomistic simulations. This was realized by utilizing the lattice trapping effect [8,18–21], which arises intrinsically due to the discrete nature of crystal lattice. For a graphene sheet containing a pre-existing crack, we identified a novel fracture mechanism, involving fracture paths of alternating bond rotation and rupture at a crack tip. Such a mechanical fracture mode has not been captured in the study of the fracture in pristine single-walled CNTs [8] and may have implications for controlling the atomic-scale morphology of fracture edges, which can significantly influence the electronic properties of graphene either intrinsically or by further edge functionalization [22,23].

As shown in Fig. 1, we adopt a size-reduced model (1910 carbon atoms in total) consisting of a small circular-shaped domain cut around a crack tip. Such a small system can effectively model a long crack that extends self-similarly under remote tensile loading. The domain size is chosen such that its outer boundary falls in the K-dominant zone. An analytical bond-order potential, denoted by BOP4S [24] is used to describe the covalent C–C interactions. This potential describes more accurately the energetics of bond rotation than the widely used Tersoff–Brenner potential [25]. To explore the dependence of our results on the specificities of interatomic potentials, we have repeated most of the simulations using the Tersoff–Brenner potential. Despite the quantitative differences, the results from the two potentials qualitatively converge. Hereafter we only present the results from the BOP4S. The in-plane elastic constants of graphene can be calculated based on the Cauchy–Born hypothesis [11]. The BOP4S potential gives the Young's modulus, Y, of 28.16 nN/Å (equivalent to the bulk value of 0.84 TPa if adopting an empirical graphene thickness of 3.34 Å), consistent with recent

* Corresponding author.
  E-mail address: suz10@psu.edu (S. Zhang).
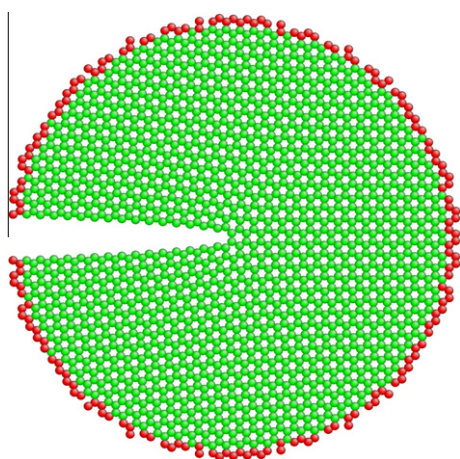
Fig. 1. A size-reduced semi-infinite crack model in a monolayer graphene loaded by a Mode-I K-field. Atoms at the outer boundary (red) are fixed, while the remaining atoms (green) are free. (For interpretation of the references to colour in this figure legend, the reader is referred to the web version of this article.)

experimental data [2] and phonon dynamics calculations [26] ($Y \sim 1$ TPa). The Poisson's ratio, v, derived from the potential, is 0.149.

To determine an equilibrium configuration of the cracked system, all the atoms in the graphene sheet are initially positioned according to the crack-tip asymptotic solution at the specified Mode-I stress intensity factor K. Atoms about 3 Å (red colored in Fig. 1[1]) from the outer boundary are held fixed, while the remaining atoms (green colored in Fig. 1) are relaxed using the limited memory Broyden–Fletcher–Goldfarb–Shanno (BFGS) geometry optimization algorithm [27].

We probe the fracture mechanisms around the Griffith load of fracture. Due to the symmetry of the hexagonal lattice, the monolayer graphene can be treated as a two-dimensional isotropic material. The Griffith load is given by $K_G = \sqrt{2Y\gamma_s}$, where γ_s is the surface energy density that can be determined by the equilibrium bond energy and the lattice constant. The BOP4S potential gives $K_{G,1}$ = 6.460 eV Å$^{-5/2}$, where the subscript '1' denotes the first step of crack extension by one atomic spacing, as shown in Fig. 2 (from a to b). In addition to the theoretical prediction, the Griffith load can also be determined numerically by finding the critical applied K^{app} value at which the net change of the total energy of the system vanishes upon unit crack extension by one lattice spacing [20]. This numerical scheme yields a Griffith load of 6.443 eV Å$^{-5/2}$. The consistency of the Griffith load between the theoretical and numerical predictions validates the numerical scheme.

Note that the Griffith criterion of fracture is based on the energy balance of two metastable states along the fracture path, which differ by one lattice spacing in crack length [28]. Crack propagation involves a sequence of such unit processes of bond breaking at the crack tip. Theoretical studies revealed that the discreteness of crystal lattices results in an atomic scale corrugation of energy landscape, which can locally trap the crack tip into a series of metastable states, a phenomenon known as 'lattice trapping' [8,18–21]. Transition from one metastable state to another along the crack propagation path requires thermally or mechanically activated crossing of the lattice trapping barrier, which depends on the characteristics of the interatomic potential and the lattice type [29,30]. The existence of lattice-trapped states allows us to capture and examine various cracking pathways in atomic details.
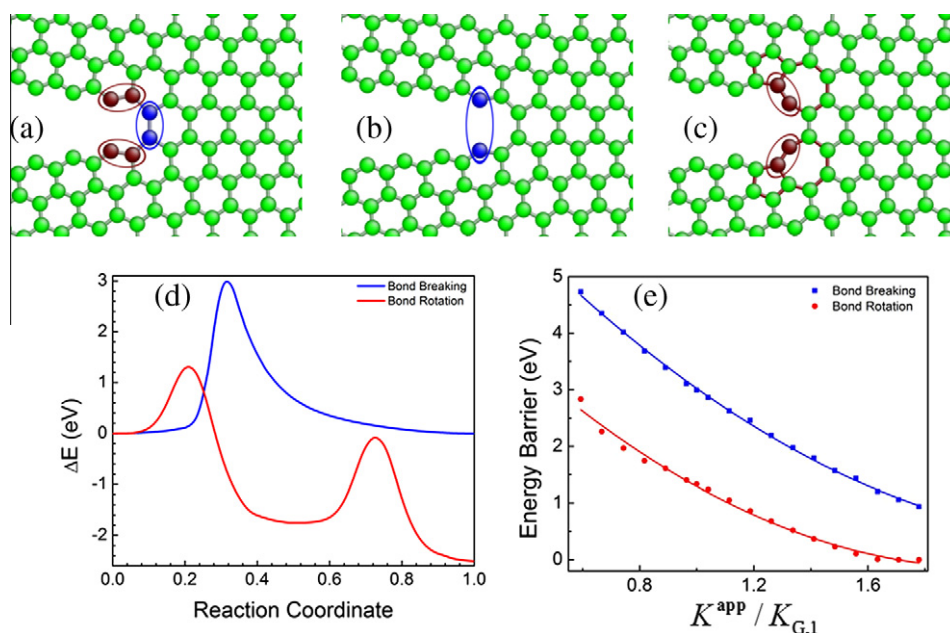
Besides the crack-tip bond breaking (Fig. 2a to b), a competing atomic process of fracture involves bond rotation (Fig. 2a to c). This bond rotation leads to formation of two 5/7 SW defects (Fig. 2c), each residing on one side of the crack surfaces. Note that the larger ring of heptagon is located closer to the crack tip than the smaller ring of pentagon. This geometrical arrangement arises from energy minimization, and enables a larger opening of the crack tip to facilitate the stress relaxation and energy release. It should be emphasized that these two fracture processes are 'rare' events when the applied load is below the athermal limit [31] and the energy barriers are much higher than the thermal energy. As a result, they may not be directly accessible to classical molecular dynamic (MD) simulations at low temperature due to the time-scale constraint. To overcome the time-scale limitation of MD, we perform the nudged elastic band (NEB) [32] calculations to determine the minimum energy paths (MEPs) for the two competing mechanisms. For the two-dimensional atomic monolayer, the MEP is a continuous path in a $2N$ dimensional configuration space (where N is the number of free atoms) among which the atomic forces are zero at any point in the $2N - 1$ dimensional hyperplane perpendicular to the path. In our NEB calculations, the initial path is represented by 10 equally spaced intermediate replicas connected by elastic springs. Nudged relaxation of the elastic band via the projected velocity Verlet method yields a discrete MEP. The calculations are considered to be converged when the force on each replica perpendicular to the path is less than 0.05 eV/Å. A continuous MEP is generated by polynomial fitting of the discrete MEP [33]. The energy barriers against bond breaking (Fig. 2a to b) and bond rotation (Fig. 2a to c) can be extracted from the saddle points on the MEPs. We have also performed classical MD simulations at elevated temperatures to directly observe the fracture processes at the crack tip. The atomic processes, studied by our NEB calculations as reported in this Letter, are representative in MD simulations.

Fig. 2d plots the MEPs for the two competing mechanisms at the Griffith load. It is seen that bond rotation is more favorable both energetically and kinetically. A similar trend has been recently observed in silicon [19]. In the MEP calculations, we treat the nucleation of two SW defects as a sequential rather than a simultaneous barrier-crossing process since the former is more kinetically favorable. Fig. 2e shows the energy barriers at various K-loads. The energy barriers for bond rotation are consistently 1–2 eV lower than those for bond breaking. This indicates that bond rotation is more kinetically favorable. The activation energy barrier for bond rotation vanishes when the applied K-load is about 10.3 eV Å$^{-5/2}$, identified as the athermal load for instantaneous bond rotation.

We have investigated the fracture of graphene beyond the first step of formation of two SW defects. Due to the presence of the SW defects, the mechanical environment local to the crack tip is considerably altered. The bond rotations significantly relax both von Mises effective shear stress and the hydrostatic stress at the crack tip (see Supplementary data). The relaxed stress field suppresses further bond breaking and rotation by increasing energy barriers and lowering the thermodynamic driving force. As a result, the Griffith load of crack extension for the SW defect-present configuration (Fig. 2c) is markedly higher than that for the dislocation-absent configuration (Fig. 2a) due to the shielding effect of defects at the crack tip. We numerically determine the Griffith load by invoking the energy balance criterion as illustrated earlier, yielding $K_{G,2}$ = 10.114 eV Å$^{-5/2}$ for the configuration shown in Fig. 2c, where the subscript '2' denotes the second step of crack extension by one atomic spacing.

Starting from the configuration shown in Fig. 2c, we have studied several kinetically possible processes, e.g., bond breaking, bond rotation-induced emission of 5/7 dislocations, and bond rotation-induced separation between the pentagon and heptagon. Here we focus on the bond breaking modes which are more kinetically

---

[1] For interpretation of colour in Fig. 1, the reader is referred to the web version of this article.

Fig. 2. Competing processes of crack-tip bond breaking and bond rotation. (a → b) Crack extension by breaking a crack-tip bond (in blue). (a → c) The brown-colored bonds are rotated by 90°, forming the 5/7 SW defect residing on each side of the crack surfaces. (d) The minimum energy paths of the two competing mechanisms at the Griffith load. (e) Load-dependent activation energy barriers. (For interpretation of the references to color in this figure legend, the reader is referred to the web version of this article.)
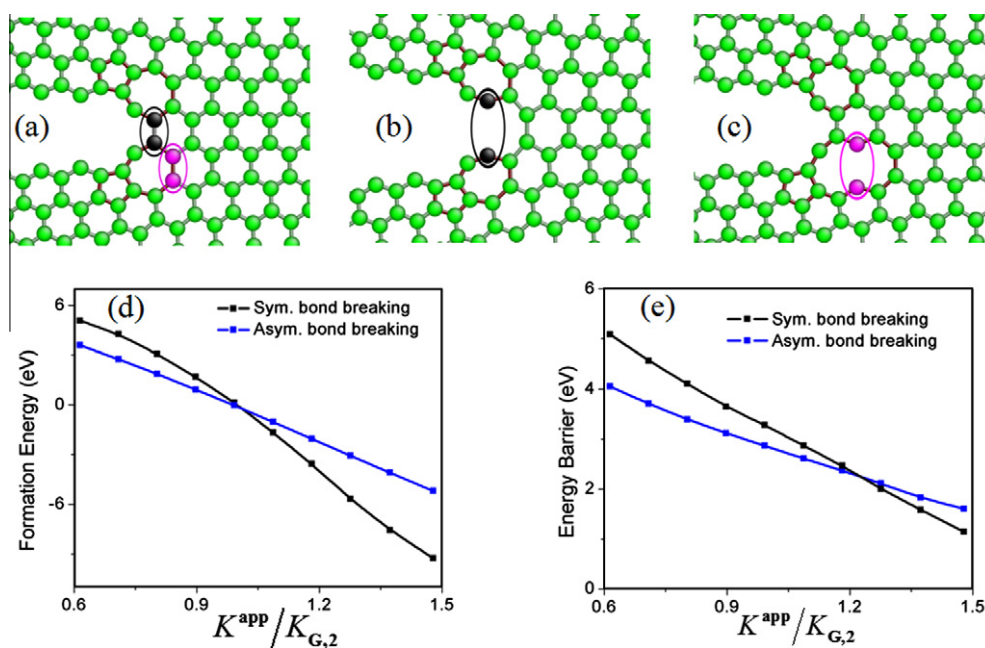
Fig. 3. Crack-tip bond breaking after the first step of bond rotation. (a) Crack tip after the first step of bond rotation. (b) Symmetric and (c) asymmetric bond breaking. (d) Load-dependent formation energies and (e) activation energy barriers from the NEB calculations.

favorable, including symmetric cleavage fracture by breaking the first bond at the crack tip (Fig. 3a to b), and asymmetric cleavage fracture by breaking the bond adjacent to the first bond at the crack tip (Fig. 3a to c). In Fig. 3d and e, we plot, respectively, the corresponding load-dependent formation energies and kinetic barriers. Fig. 3e shows that there exists a crossover point of the applied load of the two bond breaking processes, denoted by K^{cross}. The crossover of energy barriers implies the switching of the rate-limiting step. When $K^{app} < K^{cross}$, asymmetric bond breaking is more kinetically favorable; when $K^{app} > K^{cross}$, symmetric bond breaking will dominate kinetically.

Taking either Fig. 3b or c as the starting configuration, we have further investigated the crack extension pathways, as shown in Fig. 4. For clarity, Fig. 4a and b, respectively, duplicate Figs. 2a, c, and 4c, c′, respectively, corresponds to Fig. 3b and c. For the configuration in Fig. 4c, our NEB calculations show that a further bond rotation is kinetically favorable as compared to bond breaking. The bond rotation leads to the separation of the pentagon and the heptagon, and moves the heptagon toward the crack tip, see Fig. 4d. This configuration is geometrically similar to Fig. 4b except that the pentagon is moved away from the crack tip. The subsequent crack-tip response would be bond breaking, similar to the
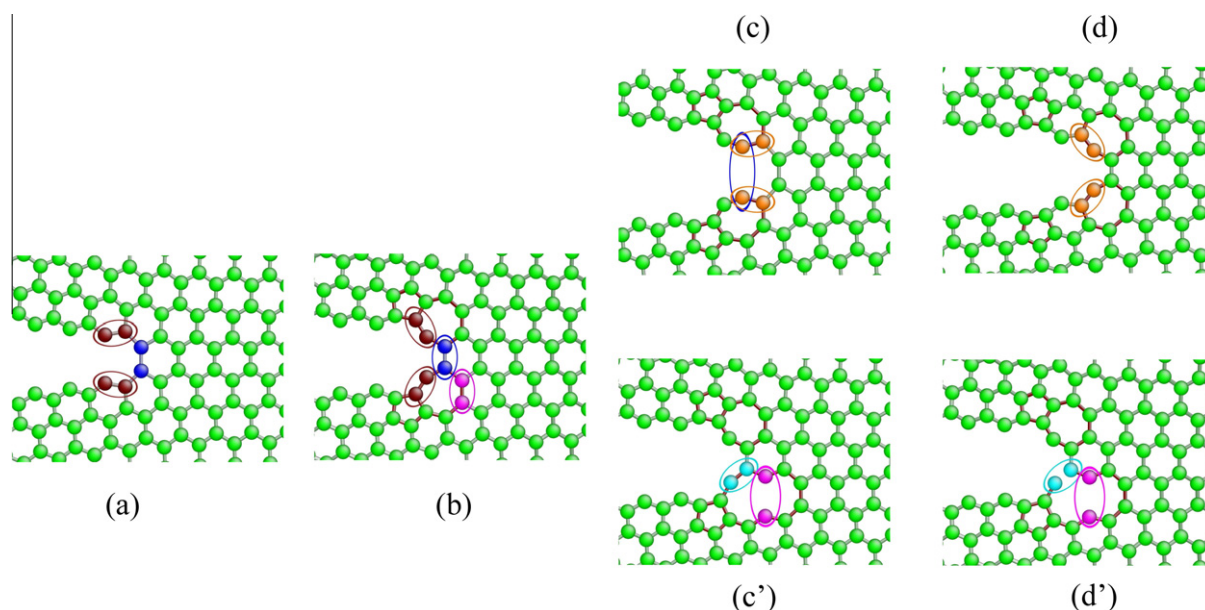
Fig. 4. Fracture paths in graphene: alternating sequence of bond breaking and bond rotation. Ovals with the same color in succeeding figures indicate the transformation process before and after bond rotation or breaking. (a → b) Bond rotation; (b → c) Symmetric bond breaking; (c → d) Bond rotation-induced separation of the pentagon and the heptagon; (b → c′) Asymmetric bond breaking: the bond adjacent to the crack-tip bond breaks; (c′ → d′) Bond breaking causes a local shift of the fracture path downward by one hexagon.

process from configuration (b) to (c). Overall, for the symmetric bond breaking process, the crack propagates by the alternating sequence of bond breaking and bond rotation in a self-similar manner, as shown in Fig. 4: a → b → c → d → b → c → d. This sequence repeats, leading to macroscopic fracture.

Taking Fig. 3d (i.e., Fig. 4c′) as the starting configuration, our NEB calculations show that one of the bonds that belongs to the large open rings is prone to breaking, see Fig. 4d′. This causes a local shift of the fracture path downward by one hexagon. The shifted crack tip is enclosed by perfect hexagons, and it is geometrically similar to Fig. 4a. Therefore, further crack extension would proceed by alternating sequence of bond breaking and bond rotation in a self-similar manner, as shown in Fig. 4: a → b → c′ → d′ → a. Because of the structural and loading symmetries, this asymmetric breaking mode can also occur by shifting the crack path upward. During a kinetic crack-growth process under quasi-static loading [34] the two pathways revealed in Fig. 4 are both kinetically possible. The overall crack extension path is expected to remain straight, as dictated by the condition of quasi-static crack growth on the plane of maximum normal stress. As a consequence, the alternating sequence of bond breaking and bond rotation can create the fracture edges with mixed five- and seven-membered rings, and the asymmetric bond breaking can lead to the atomic-scale roughness of fracture edges. Of course, the dynamic effect in a fast fracture could cause crack kinking or branching, beyond the scope of this research [35].

In conclusion, we show that the fracture of a monolayer graphene can involve an alternating sequence of bond rotation and bond breaking under the quasi-static loadings around the Griffith limit of fracture. Such a fracture mode is kinetically preferred, as verified by using different interatomic potential models. However, it requires a further study using the first-principles modeling, and more importantly, through fracture experiment with high-resolution imaging. The fracture of graphene can be further manipulated by imposing mixed modes of far-field loading, including in-plane and out-of-plane shear. The mechanical cracking of graphene can create the unique atomic-scale morphologies of fracture edges fun-

damentally because of the non-uniform bond deformation and rupture at the crack tip with localized high stresses. This non-uniformity may open up an opportunity to create reconstructed edges that provide a structural basis of tailoring the electronic properties of graphene, either intrinsically or through further edge functionalization.

Acknowledgements

Appendix A. Supplementary data

Supplementary data associated with this article can be found, in the online version, at doi:10.1016/j.cplett.2010.05.090.

References

[1] K.S. Novoselov et al., Science 315 (2007) 1379.
[2] C. Lee, X.D. Wei, J.W. Kysar, J. Hone, Science 321 (2008) 385.
[3] J.S. Bunch et al., Science 315 (2007) 490.
[4] X.L. Li, X.R. Wang, L. Zhang, S.W. Lee, H.J. Dai, Science 319 (2008) 1229.
[5] T. Zhu, J. Li, S. Ogata, S. Yip, MRS Bull. 34 (2009) 167.
[6] H.E. Troiani, M. Miki-Yoshida, G.A. Camacho-Bragado, M.A.L. Marques, A. Rubio, J.A. Ascencio, M. Jose-Yacaman, Nano Lett. 3 (2003) 751.
[7] T. Dumitrica, T. Belytschko, B.I. Yakobson, J. Chem. Phys. 119 (2003) 1281.
[8] T. Dumitrica, M. Hua, B.I. Yakobson, Proc. Natl. Acad. Sci. USA 103 (2006) 6105.
[9] T. Dumitrica, B.I. Yakobson, Appl. Phys. Lett. 84 (2004) 2775.
[10] M.B. Nardelli, B.I. Yakobson, J. Bernholc, Phys. Rev. Lett. 81 (1998) 4656.
[11] S. Zhang, T. Zhu, Philos. Mag. Lett. 87 (2007) 567.
[12] B.I. Yakobson, Appl. Phys. Lett. 72 (1998) 918.
[13] J.Y. Huang, F. Ding, B.I. Yakobson, Phys. Rev. Lett. 100 (2008) 035503.
[14] J.Y. Huang et al., Phys. Rev. Lett. 94 (2005) 236802.
[15] D. Bozovic, M. Bockrath, J.H. Hafner, C.M. Lieber, H. Park, M. Tinkham, Phys. Rev. B 67 (2003) 033407.
[16] S.L. Zhang, S.L. Mielke, R. Khare, D. Troya, R.S. Ruoff, G.C. Schatz, T. Belytschko, Phys. Rev. B 71 (2005) 115403.
[17] A.J. Stone, D.J. Wales, Chem. Phys. Lett. 128 (1986) 501.
[18] J.E. Sinclair, Philos. Mag. 31 (1975) 647.

[19] S. Huang, S.L. Zhang, T. Belytschko, S.S. Terdalkar, T. Zhu, J. Mech. Phys. Solids 57 (2009) 840.
[20] S.L. Zhang, T. Zhu, T. Belytschko, Phys. Rev. B 76 (2007) 094114.
[21] R. Thomson, C. Hsieh, V. Rana, J. Appl. Phys. 42 (1971) 3154.
[22] J.Y. Huang, F. Ding, B.I. Yakobson, P. Lu, L. Qi, J. Li, Proc. Natl. Acad. Sci. USA 106 (2009) 10103.
[23] V.B. Shenoy, C.D. Reddy, A. Ramasubramaniam, Y.W. Zhang, Phys. Rev. Lett. 101 (2008) 245501.
[24] D.G. Pettifor, I.I. Oleinik, Phys. Rev. Lett. 84 (2000) 4124.
[25] D.W. Brenner, O.A. Shenderova, J.A. Harrison, S.J. Stuart, B. Ni, S.B. Sinnott, J. Phys.-Condens. Matter 14 (2002) 783.
[26] F. Liu, P.M. Ming, J. Li, Phys. Rev. B 76 (2007) 064120.

[27] J.C. Gilbert, J. Nocedal, Appl. Math. Lett. 6 (1993) 47.
[28] T. Zhu, J. Li, S. Yip, Phys. Rev. Lett. 93 (2004) 205504.
[29] W.A. Curtin, J. Mater. Res. 5 (1990) 1549.
[30] T. Zhu, J. Li, S. Yip, Proc. Roy. Soc. Lond. A462 (2006) 1741.
[31] A.S. Argon, Scr. Metall. 16 (1982) 259.
[32] H. Jonsson, G. Mills, K.W. Jacobsen, in: B.J. Berne, G. Ciccotti, D.F. Coker (Eds.), Classical and Quantum Dynamics in Condensed Phase Simulations, World Scientific Publishing Company, 1998, pp. 385–404.
[33] G. Henkelman, H. Jonsson, J. Chem. Phys. 113 (2000) 9978.
[34] J.R. Rice, J. Mech. Phys. Solids 26 (1978) 61.
[35] M.J. Buehler, H.J. Gao, Nature 439 (2006) 307.